J. Rapp, G. Pintsuk, Ph. Mertens, H. Altmann, P.J. Lomas, V. Riccardo
and JET EFDA contributors

Geometry and Expected Performance of the Solid Tungsten Outer Divertor Row in JET

Geometry and Expected Performance of the Solid Tungsten Outer Divertor Row in JET

J. Rapp[1,2], G. Pintsuk[3], Ph. Mertens[1], H. Altmann[4], P.J. Lomas[4], V. Riccardo[4]
and JET EFDA contributors*

JET-EFDA, Culham Science Centre, OX14 3DB, Abingdon, UK

[1]*IEF-4, Forschungszentrum Jülich, EURATOM Association, Trilateral Euregio Cluster, Jülich, Germany*
[2]*FOM Rijnhuizen, EURATOM Association, Trilateral Euregio Cluster, Nieuwegein, The Netherlands*
[3]*IEF-2, Forschungszentrum Jülich, EURATOM Association, Trilateral Euregio Cluster, Jülich Germany*
[4]*EURATOM-UKAEA Fusion Association, Culham Science Centre, OX14 3DB, Abingdon, OXON, UK*
* See annex of F. Romanelli et al, "Overview of JET Results",
(Proc. 22 [nd] IAEA Fusion Energy Conference, Geneva, Switzerland (2008)).

ABSTRACT.

At JET new plasma-facing components for the main chamber wall and the divertor are being designed and built to mimic the expected ITER plasma wall conditions in the deuterium-tritium operation phase. The main wall elements at JET will be made of beryllium and the divertor plasma-facing surface will be made of tungsten. Most of the divertor tiles will consist of tungsten-coated Carbon Fibre Composite (CFC) material. However one toroidal row in the outer divertor will be made of solid, inertially cooled tungsten. The geometry of these solid tungsten divertor components is optimized within the boundary conditions of the interfaces and the constraints given by the electrodynamical forces. Shadowing calculations as well as rough field line penetration analysis is used to define the geometry of the tungsten lamella stacks. These calculations are based on a set of magnetic equilibria reflecting the operation domain of current JET plasma scenarios. All edges in poloidal and toroidal direction are shadowed to exclude near perpendicular field line impact. In addition, the geometry of the divertor structure is being optimized so that the fraction of the plasma wetted surface is maximised. On the basis of the optimized divertor geometry, performance calculations are done with the help of ANSYS to assess the maximum power exhaust possible with this inertially cooled divertor row.

1. INTRODUCTION

For ITER [1] and later for DEMO tungsten is foreseen to be a potential plasma facing material in the divertor and in the case of DEMO also in the main chamber, mainly due to its low physical sputtering rate and high melting temperatures. In order to study the effect of a tungsten divertor on the plasma performance, material transport and fuel retention the ITER-like wall project [2] has been started in 2005 at JET to mimic the ITER material mix foreseen for the Deuterium/Tritium operational phase. In the frame of this ITER-like wall project, a new row of divertor tiles has been developed, which consists of 96 bulk tungsten 'tile modules', to replace the present Load-Bearing Septum Replacement Plates (LBSRP). Figure 1 shows the bulk tungsten divertor row in JET. A lamella design has been chosen to be compatible with the thermo-dynamical and disruption electromagnetic forces during disruptions. 4 stacks of lamella are mounted as one 'tile module' on a carrier. Each carrier will hold two 'tile modules' and hence 8 stacks of lamellas. Figure 2 shows the arrangement of the 8 stacks on one carrier. The number of carriers (48) is given by the Mk-II divertor structure and attachments as well as remote-handling constraints.'

In section 2 the toroidal shadowing of the divertor tiles is determined and in section 3 the poloidal shadowing of the divertor tiles is calculated. In section 4 the performance of the divertor is estimated.

2. TOROIDAL SHADOWING OF TILES

The chamfering of all tiles and lamellae in toroidal direction should ensure that all leading edges are shadowed for a given set of magnetic field line configurations. These magnetic plasma (magnetic field line) configurations are calculated by a predictive equilibrium code named PROTEUS [3].

This set of configurations was also used previously for the design of the present LBSRP [4, 5]. All configurations were scaled to the lowest edge safety factor sensible at JET (q_{95} of 2, 3) leading to the largest field line angle to the wall components. The field line angle with its components $\theta_\perp$ and $\theta_\parallel$ are shown in figure 3. This section covers mainly the tilt of the stack of lamellae to each other. However, also the individual lamellae are shadowed of course.

In addition to the number and size of gaps between the stacks, tolerances of the individual divertor components (carrier, lamellae etc.) determine the performance of the divertor. In table 1 and table 2 the tolerances of the divertor components are summarized, x is in toroidal direction, y is in radial (poloidal) direction and z is perpendicular to x-y plane. As mentioned above the two 'tile modules' are mounted on one carrier. This means that the tolerances on the common carrier are smaller, because relatively to each other the errors are only determined by the fabrication tolerance of the lamellas and the stack mounting tolerances.

The sizes of the gaps are defined by the remote handling boundary conditions. The gap g_1 between carriers is 13mm and the gap g_2 between two toroidal adjacent stacks on the same carrier is 11mm. The tolerances in the gaps have been taken into account. As a consequence of the different gap sizes and the different tolerances on the carrier and between carriers the chamfer angle ± should be different too, as indicated by the schematic drawing in figure 4. However, the chamfer angle ± is kept constant in order to keep the power flux density on the surface the same on the expense of an optimized toroidal wetted fraction.

The design of the LBSRP does foresee a poloidal varying inclination angle for optimized stack to stack shadowing. This is a result of the maximum $\theta_\perp$ since $\theta_\perp$ varies with the radial position of the outer strike point and is lower the closer it is to the X-point. The $\theta_\perp$ is shown for all relevant magnetic configurations in figure 5. The chamfer angle is lowest for stack1 and highest for stack4. It is designed to shadow toroidally for configurations with $\theta_\perp = 3^\circ$ (stack1); 4° (stack2); 5.5° (stack3) and 6.5° (stack4). Figure 6 illustrates the radial (poloidal) different chamfers angles of the stacks.

The optimized chamfer should lead to a maximized Toroidal Wetted Fraction (TWF), which is generally defined in the following:

$$ \tag{1} $$

In this expression we refer only to the toroidal wetted fraction due to the tilt of the individual stacks or tiles. Changes in the wetting fraction due to local effects depending on the geometry of the lamellae are discussed in section 4.

For small angles of α the following expression is more accurate for a different chamfer between carriers or on common carriers:

$$ \tag{2} $$

2

Here cos α is typically close to 1 and can be neglected. The index x refers to the gap between carriers and on common carriers and the 'tile', including angle α, following this gap (see figure 4). The difference between the optimized and non-optimized chamfering (chamfer angle for $\theta_\perp = 6.5°$ for all stacks) is demonstrated in figure 7. For the optimized chamfering an increase in the toroidal wetted fraction of more than 20% can be achieved on stack1. The results for the optimized chamfering are summarized in table 3. In figure 8 the difference in the toroidal wetted fraction of the CFC tile LBSRP and the W LBSRP are shown. The main reasons for the reduced TWF are the larger tolerances for the tungsten divertor and the gaps between the lamellas of 1mm (6mm/7 mm). Those gaps lead to a reduction of the TWF to 87%, which is consistent with the TWF at large radii where the $\theta_\perp$ is largest, and hence the difference in the tolerances has negligible impact on the TWF.

The details of the lamella design impact on the maximum possible $\theta_\perp$ at a particular radial position for $q_{95} = 2.3$. For a 0.7mm rounded edge (with a radius of 5mm) at the back end of the lamella this edge reduces the shadowing height by 0.05mm. But the 3.8mm rounded edge (radius 14.5mm) on the front face increases the shadowed depth by 0.5mm. This altogether leads to an increase of the maximum allowed $\theta_\perp$ of more than 20% (see figure 9).

3. POLOIDAL SHADOWING OF TILES

In addition to the toroidal tilt, the stacks need to be chamfered in poloidal direction. Figure 10 shows the step from stack to stack in poloidal direction for a poloidal gap of 1mm, calculated with $\theta_\perp$ and $\theta_\parallel$ for $q_{95} = 2.3$ and the tolerances as given in table 2. For most configurations the necessary step is between 0.5 mm and 1.5mm at the strike point. However, magnetic field lines in the Scrape-Off-Layer (SOL) require a larger poloidal chamfer. The magnetic field lines of up to a $\Delta_\Psi = 2cm$ (distance of flux surfaces in flux coordinates taken on the outer midplane, omp) should be covered. The power flux density for $\Delta_\Psi = cm$ is reduced to 1.8 % of the peak power flux at the strike point, assuming a power decay length of 5mm-omp. The poloidal step necessary to avoid penetration at $\Delta_\Psi = 2cm$ is 1.9mm. Including the tolerances for stacks on common carriers this leads to a poloidal step of 2.5mm.

Even with perfect toroidal and poloidal shadowing a field line can penetrate in one of the poloidal gaps and sink down significantly below the top surface of the lamellae. This involves the risk of exposing a toroidal facing area on tile C or D. Within the gaps the lamellas are chamfered to each other, creating a funnel. The main problem is the penetration of field lines with low $\theta_\perp$ along the gap and then the interception of the toroidally facing edge of the next lamella stack. This is illustrated in figure 11. A field line could penetrate the gap between tiles stacks A and C drop in this channel and in the worst case hit with almost perpendicular field line angle a lamella on tile (stack D). In figure 12 this drop of a field line is illustrated with a section along the field line. The geometry, chamfering has to accommodate for those field line penetrations. Simple calculations have been performed to check for this effect under the assumptions that $\theta_\parallel$ does not vary during the field line drop. The following calculations have been performed for a poloidal gap of 1mm. The field line

drop in the poloidal gap h is up to 3mm for a few configurations (see figure 13). The height difference between the poloidal neighbouring tiles is 2.5mm from the poloidal chamfering and 1.7mm−0.8mm (between carriers) or 1.3mm−0.6mm (common carrier) from the toroidal chamfering (minus the tolerances) of the neighbouring tiles, resulting in a step from the tile A of stack$_x$ to tile D of stack^{x+1} of 3.3mm or 3.1mm respectively. Essentially this means that the front face of the first lamella of a stack needs an additional chamfer in the order of 0.4mm. But as shown in section 2 the details of the lamella design lead to an increase of the shadowed depth by about 0.45mm consistent with the requirements given above.

4. PERFORMANCE CALCULATIONS

The performance target of the divertor is to enable a power exhaust of 40MW total input (heating) power for 10s. The performance of the divertor is calculated under the assumption of the following boundary conditions.

- 30% of the heating power is radiated.
- The power sharing between the outer and inner divertor leg is 2.5:1
- The power decay length λ in the SOL in the outer mid-plane is 5mm.
- The critical temperature of W sublimation is 3200°C. But some margin is required, for instance with respect to material re-crystallization, and a maximum temperature of 2800°C is assumed in this first step. Please note that re-crystallization can occur already at much lower temperatures. But those details of the re-crystallization are not further discussed in here.

A number of 2D finite element (ANSYS [6]) simulations have been carried out to study the influence of the field line angle $\theta_\perp$ and the stack angle α on the wetted fraction of the lamella due to the surface geometry of each individual lamella. Figures 14 and 15 show an example of a lamella exposed to a power flux density of $q = 10$MW/m^2 for two different lamella wetted fractions. Figure 16 shows the maximum surface temperature after 10s for different impact angles and different power flux densities. The starting temperature is 200°C. The 2D ANSYS data are normalized to 3D calculations. The important result is that the maximum temperature does not differ between the cases of 1° and 8° impact angle. This is an indication that the heat conduction of tungsten is good enough in toroidal direction so that the change in (lamella wetted fraction) LWF on the lamella between 45% and 75% does not matter. Only for angles of 0.5^o a deviation is observed and local overheating leads to higher temperatures. Since the minimum of $\theta_\perp + \alpha$ is about 0.5^o + 0.43^o is only slightly lower than the 1°, the detailed design of the lamella surface will not restrict the power handling. The maximum temperature on the lamella scales with $(q \times LWF)^{0.67}$.

However, the 3D ANSYS calculations reveal a linear dependence of the temperature on the impacting heat flux. Figure 17 shows the maximum temperature as function of the impacting heat flux for a flux expansion of 4. This is equivalent to a power decay length λ on the target of 20mm, meaning 4 times the power decay length in the outer mid-plane. As a reference, for ITER a flux

expansion of 7 will be typical. For those configurations (flux expansion of 4) the maximum temperature of 2800$^{\mathrm{o}}$C is reached at q×LWF = 18MW/m^2, regardless of the impact angle and hence the Lamella Wetted Fraction (LWF). For those heat fluxes (18MW/m^2) a temperature of about 800$^{\mathrm{o}}$C at the supporting structures (approximately 2cm below the lamella surface) is reached. For high flux expansions the critical temperature for the supporting structure is already reached at lower heat flux densities. Figure 18 shows the max. temperature after 10s exposure to a heat flux of 20MW/m^2 with an incident angle of 1$^{\mathrm{o}}$ for flux expansions of 4, 25 and infinity. The maximum temperature roughly scales with s the square root of the ratio of the average heat flux density to the peak heat flux density:

$$ \tag{3} $$

with the peak and average heat flux densities given like:

$$ \tag{4} $$

$$ \tag{5} $$

where l is the length of the lamella in radial direction (60mm), λ is the power decay length in the outer mid-plane (here 5mm) and F is the flux expansion on the target. A better scaling would be:

$$ \tag{6} $$

On the basis of those ANSYS calculations and the derived dependencies on wetted fraction, peak heat flux and average heat flux performance calculations have been carried out.

Figure 19 shows the power handling of all configurations with static strike points for a critical surface temperature of 2800$^{\mathrm{o}}$C. Clearly configurations with a high flux expansion, like 4MA_hdlx, lead to a better power handling of the W-LBSRP. In table 4 the results of the power handling for the static configurations are summarized. For most of the configurations the tungsten surface temperature is limiting the maximum heating power or pulse length. The maximum heating power is mostly below the performance target of 40MW for 10s.

The critical time to reach the surface temperature of 2800$^{\mathrm{o}}$C can be increased by strike point sweeping, thus distributing the power load on poloidally adjacent stacks. The averaged power profiles were taken from earlier calculations for the design of the CFC LBSRP [7]. The maximum surface temperature of 2800$^{\mathrm{o}}$C is reached with a heat flux density of 14MW/m^2.

But the limitation of the pulse length for a heating power of 40MW is now in all cases the temperature of the support structure instead of the lamella surface temperature, thus providing an energy limit. For a maximal surface temperature of 2800$^{\mathrm{o}}$C the pulse length for all configurations is

much beyond 10s. But the maximal temperature of 700°C for the support structure is already reached at an average power flux density of 8MW/m^2. These ANSYS calculations are in good agreement with some experimental results obtained at JUDITH [8]. Both limitations are listed in table 5. Comparing table 4 with table 5 reveals, that for some configurations the critical time until the bulk temperature reaches 700°C is not larger for swept configurations than for static configurations. For the 3MA5_hd, 4MA_hd, 4MA_hd2 and 4MA_hdlx the performance target is reached.

The power handling of the W-divertor is generally acceptable and not very different from the CFC-LBSRP. However, the alignment of the lamellas in the stack is a critical issue and could in principle limit the power handling capabilities of the divertor. Figure 20 shows an illustration on the basis of some ANSYS calculations for such a stack of misaligned tungsten lamellas. Here are some examples: (1) 20MW/m^2, LWF = 60%; (2) 30MW/m^2, LWF = 90%; (3) 12MW/m^2, LWF = 75% and (4) 16MW/m^2, LWF = 100%. Obviously for the high heat flux densities the temperature could become very high. Please note that 4800°C is a theoretical value, since the melting point is at 3400°C, and should only illustrate the effect of the local heat fluxes. In the following the influence of the tolerances (fabrication and assembly) is estimated. For a simple lamella design (see figure 21) the change in the power handling has been calculated for several impact angles. Please note that the 1° is the lowest impact angle for operation scenarios, which will be actually run. Table 6 shows the increase of the local heat flux of the misaligned lamellas X. Clearly, one should aim for a reduction of the lamella tolerances to ±0.05mm in order to limit the additional temperature increase. In figure 22 the maximum input power with lamella tolerances of ±0.05mm are shown for static plasma configurations. Figure 22 reveals that for all configurations the power handling of the divertor is reduced. For some configurations this reduction has stronger implications: 4MA_hd, 4MA_hdhx, 5MA_hd and 2MA5_hbhd. For all these configurations, either the pulse length has to be restricted (<10 sec) or the radiative power fraction has to be increased.

SUMMARY AND CONCLUSION

The detailed geometry of the new JET solid tungsten divertor has been evaluated to ensure shadowing of all leading edges of the divertor. On the basis of this detailed geometry performance calculations have been performed. As expected the tolerances play an important role in the power handling of the divertor. The performance target of 40MW for 10s can only be reached in swept configurations for some of the plasma configurations, assuming a limit of the surface temperature of 2800°C and a limit of the support structure of 700°C. However, taking into account individual lamella tolerances can reduce the performance significantly. It is recommended to increase the radiative power fraction for those configurations to at least 65%, which would allow for most static configurations to operate close to the performance target of 40MW for 10s. Taking into account a safety margin would require even higher radiative power fractions or a performance below the target.

Adding a safety margin is highly recommended also in view of the thermo-mechanical stresses on the carrier structure [9].

REFERENCES

[1]. Aymar R., Barabaschi P. and Shimomura Y. (2002) Plasma Phys. Control. Fusion **44**, 519

[2]. Pamela J., et al. (2007) J. Nucl. Mater. **363-365**, 1

[3]. Albanese R., Blum J., De Barbieri O., in Computational Physics (Proc. 8th Eur. Conf. Bad Eibsee, 1986), Vol. 10D, European Physical Society (1986).

[4]. Chappuis P., et al. (2003) Fusion Engineering and Design **66-68**, 407

[5]. Salavy J.-F., Chappuis P., Lomas P.J., V. Riccardo (2005) Fusion Engineering and Design **75-79**, 505

[6]. Moaveni S. (1999) Finite element analysis: theory and application with ANSYS, Prentice Hall, Upper Saddle River, NJ, USA

[7]. Salavy J.-F. (2003) JET report

[8]. Hirai T., et al. (2007) Phys. Scr. T128, 144

[9]. Mertens Ph., et al. (2008) accepted by J. Nucl. Mater.

Between carriers	X [mm]	Y [mm]	Z [mm]
Carrier location	± 0,30	± 0,15	
CFC carrier baseplate	± 0,13	± 0,13	± 0,10
Adapter plate	± 0,20	± 0,20	± 0,05
Wedge carrier surface	± 0,05	± 0,05	± 0,05
Stack location			± 0,20
Lamella	± 0,10	± 0,10	± 0,10
Error margin	± 0,02	± 0,02	± 0,10
Total W LBSRP	± 0,80	± 0,65	± 0,60
Worst case	1,6	1,3	1,2

Table 1: Tolerances of the tungsten LBSRP for shadowing of tiles between carriers

Common carrier	X [mm]	Y [mm]	Z [mm]
Stack location			± 0,20
Lamella	± 0,10	± 0,10	± 0,10
Error margin	± 0,05	± 0,05	± 0,00
Total W LBSRP	± 0,15	± 0,15	± 0,30
Worst case	0,3	0,3	0,6

Table 2: Tolerances of the W-LBSRP for shadowing of tiles on a common carrier

	h₁ [mm]	h₂ [mm]	α₁ [º]	α₂ [º]
Stack1	2,0	1,2	0,58	0,58
Stack2	2,2	1,4	0,64	0,64
Stack3	2,6	1,7	0,74	0,74
Stack4	2,9	1,9	0,81	0,81

Table 3: Shadowing data for the lamellae stacks of the W-LBSRP.

Configuration	P_{max} [MW] $T_{surf} = 2800^oC$	P_{max} [MW] $T_{bulk} = 700^oC$	t_{crit} [s], 40MW $T_{surf} = 2800^oC$	t_{crit} [s], 40MW $T_{bulk} = 700^oC$
1MA5_hd	18.9	19	2.4	2.3
2MA5_hbhd	19.2	24.2	2.5	3.7
3MA5_hd	27.1	25.7	4.9	4.1
3MA5_ITER	23.0	25.3	3.7	4.0
4MA_hd	28	27	5.2	4.5
4MA_hd2	29.7	27.4	5.9	4.7
4MA_hdhx	23.2	28.2	3.6	5.0
4MA_hdlx	46.1	35.8	14.1	8.0
5MA_hd	32.7	28.8	7.1	5.2
Extreme	18.9	24.2	2.4	3.7
H_4MA5_LT	27.8	26.5	5.1	4.4
HT3 modified	33.7	28.9	7.6	5.2

Table 4: Power handling of the W-LBSRP with static plasma configurations: maximum power to reach a critical surface or bulk temperature after a 10 sec plasma pulse; maximum time to reach a critical surface or bulk temperature with a plasma pulse of 40 MW heating power.

Configuration	Critical time (40MW) [s] $T_{surf} = 2800^oC$	Critical time (40MW) [s] $T_{bulk} = 700^oC$
1MA5_hd	12.5	4.1
2MA5_hbhd	31	6.0
3MA5_hd	27.1	8.8
3MA5_ITER	14.5	6.8
4MA_hd	27.1	8.8
4MA_hd2	31.6	14.3
4MA_hdlx	17.9	9.75
5MA_hd	13.8	4.5

Table 5: Power handling of the W-LBSRP of swept plasma configurations: maximum time to reach a critical surface or bulk temperature with a plasma pulse of 40 MW heating power.

$\theta_\perp + \alpha$	Lamella tolerance ± 0.1mm	Lamella tolerance ± 0.05mm
1º	2.6	1.8
1.6º	2.0	1.5
4º	1.4	1.2

Table 6: Enhancement factors for the power flux due to misalignment of individual lamellae resulting from a manufacturing lamella tolerance for three different impact angles.
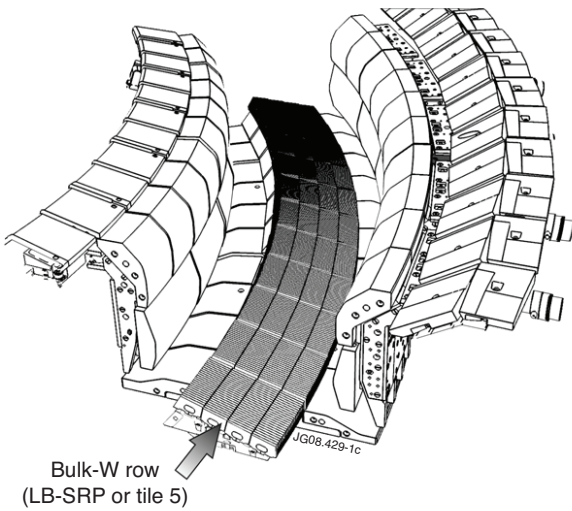
Figure 1: Rows of solid tungsten tiles in the JET divertor.
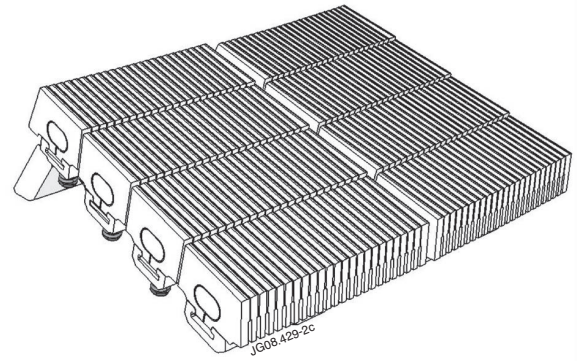
Figure 2: Drawing of one carrier with two 'tiles' and eight stacks of solid tungsten lamellae.
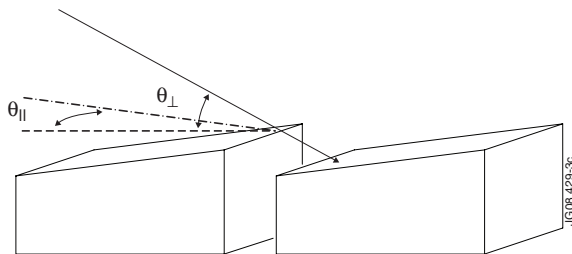
Figure 3: Schematic drawing to show the field line angles $\theta_\perp$ and $\theta_{||}$.
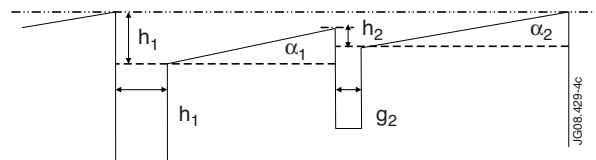
Figure 4: Schematic drawing to illustrate the shadowing of the tiles at gap 1, between carriers, and tiles at gap 2 on a common carrier.
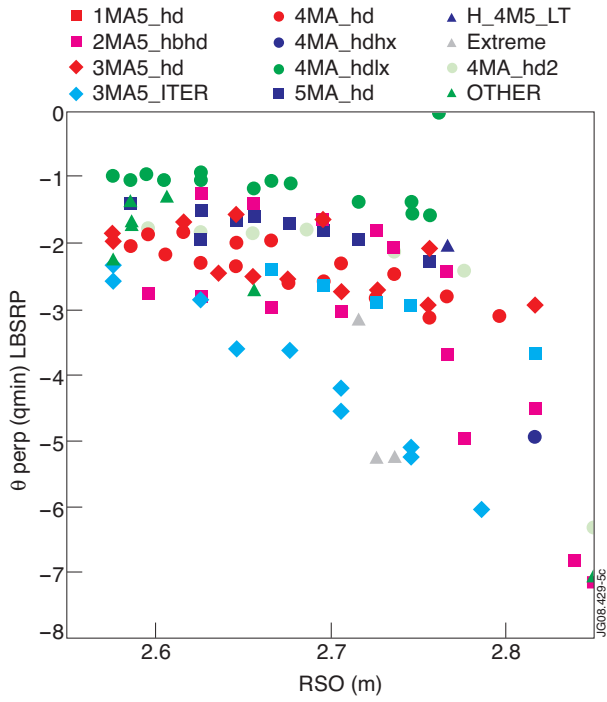
Figure 5: $\theta_\perp$ on the tungsten LBSRP for $q_{95} = 2.3$ as a function of the radial strike point position for the different magnetic plasma configurations.
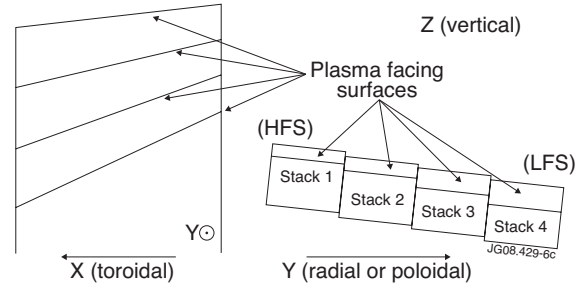
Figure 6: Schematic drawing of the 4 lamellae stacks in a toroidal and radial projection.
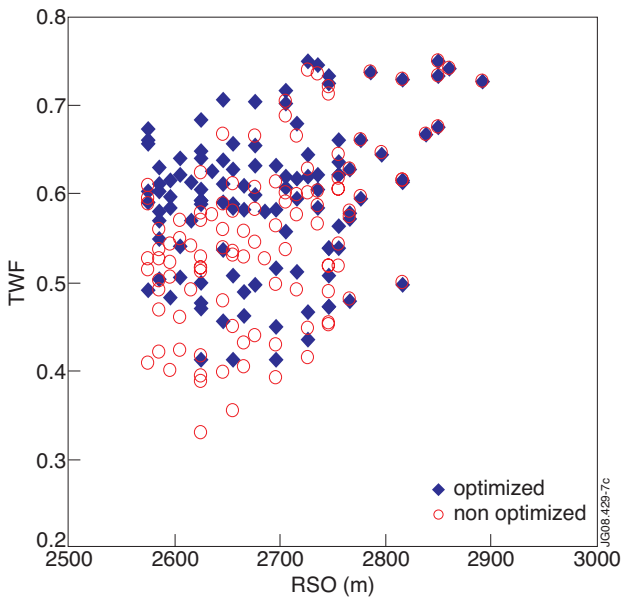
Figure 7: Toroidal Wetted Fraction (TWF) as function of the major radius for different magnetic plasma configurations: comparison of non-optimized shadowing (with a common tile angle for all 4 stacks) and optimized shadowing (with a radially varying tile angle for the 4 stacks).
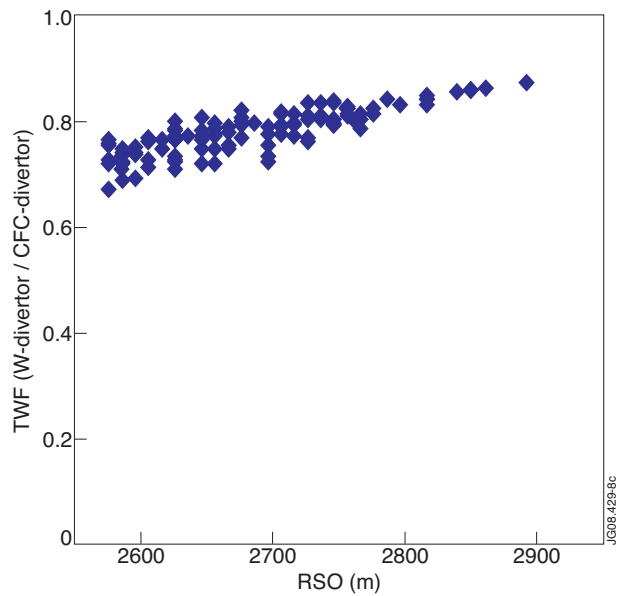
Figure 8: Ratio of the toroidal wetted fraction on the W-LBSRP and the CFC-LBSRP.
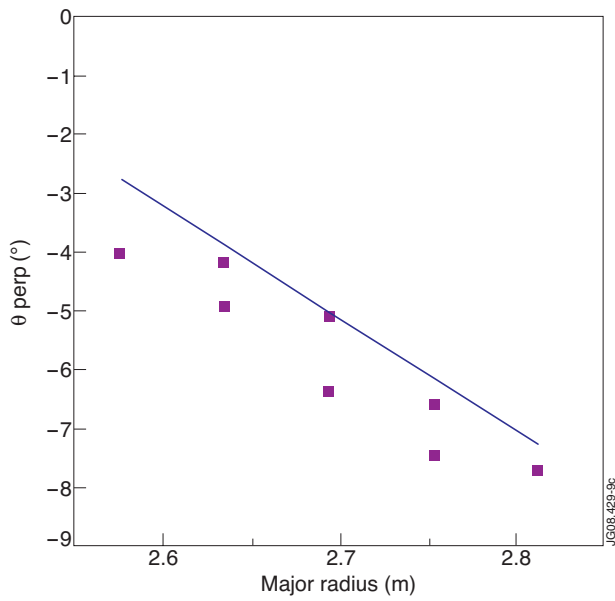
Figure 9: maximum $\theta_\perp$ on the tungsten LBSRP for $q_{95} = 2.3$ as a function of the radial strike point position taking into account the shadowing according to table 3 and the detailed lamella design.
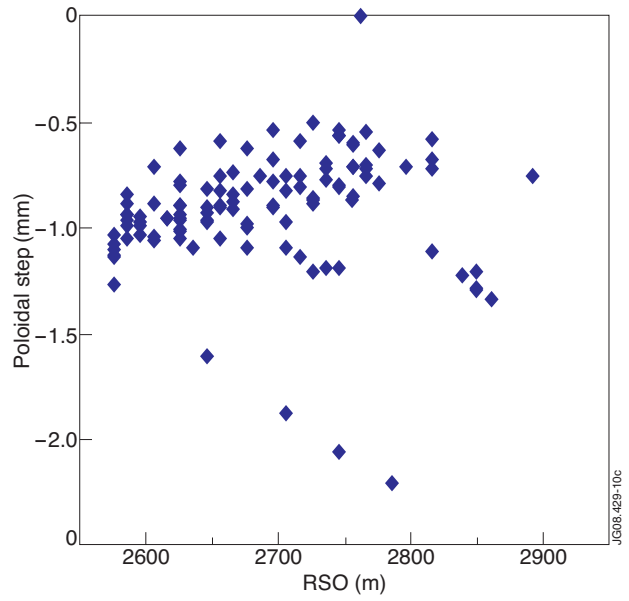
Figure 10: Step from lamella to lamella in radial (poloidal) direction to ensure shadowing of lamellae in poloidal direction: poloidal step.
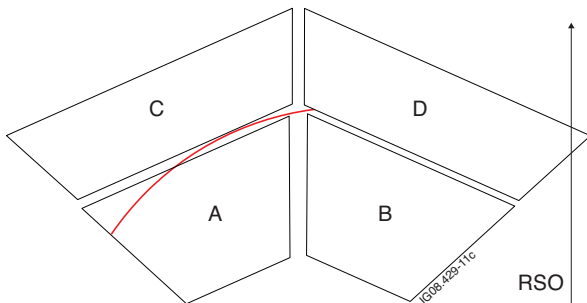
Figure 11: Schematic drawing of a field line penetrating a toroidal gap between tiles A and C and hitting tile D.
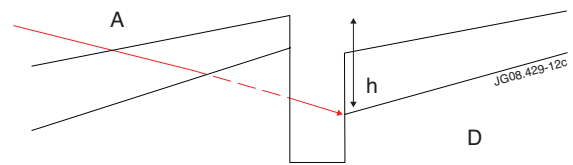
Figure 12: Schematic drawing of a field line dropping in a gap between tiles A and C and hitting tile D.

11
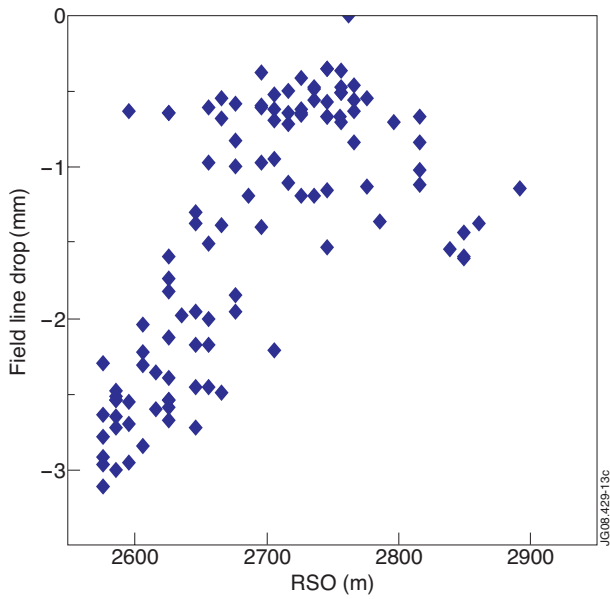
Figure 13: Field line drop in a toroidal gap between two poloidal adjacent tiles before hitting the toroidal adjacent tile.
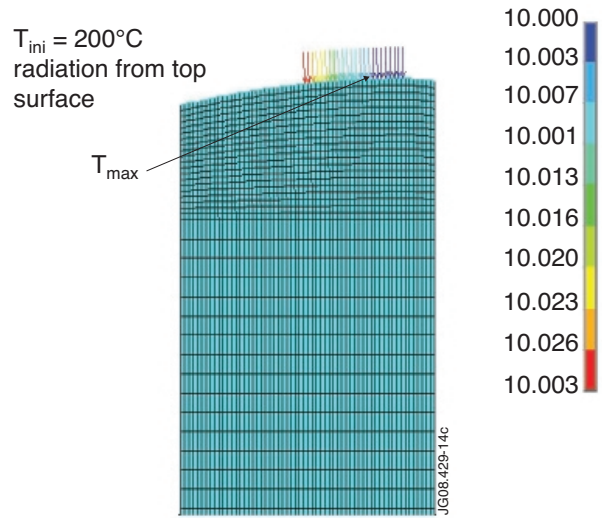
Figure 14: Grid in a lamella for the 2D ANSYS calculation with a heat flux density of 10MW/m^2 for a 45% lamella wetted fraction.
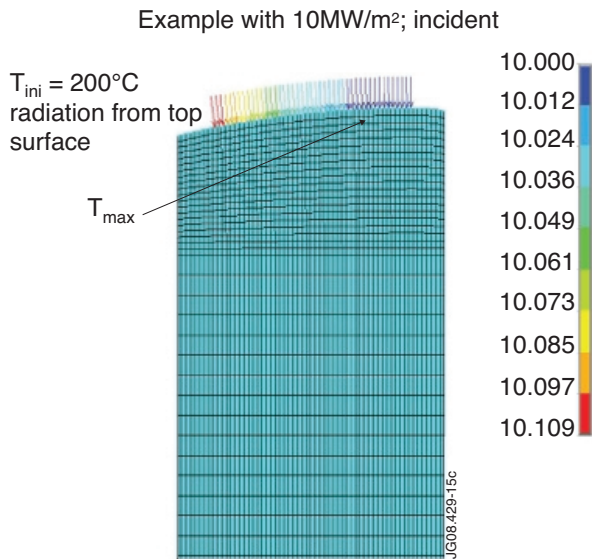
Figure 15: Grid in a lamella for the 2D ANSYS calculation with a heat flux density of 10MW/m^2 for a 75% lamella wetted fraction.
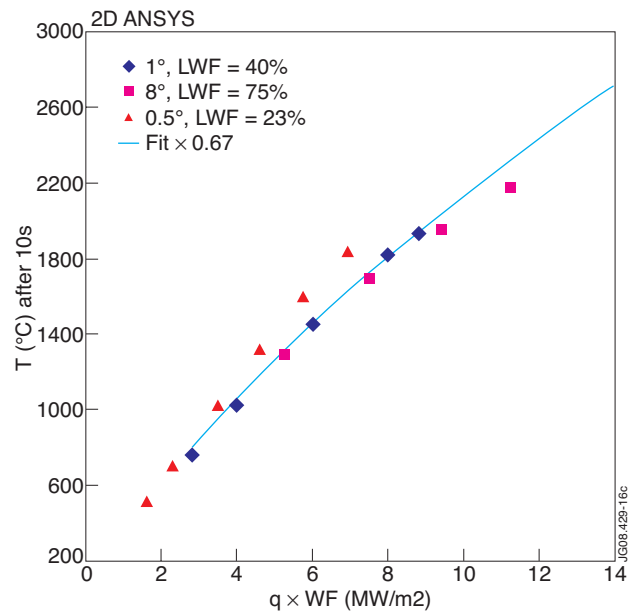

Figure 16: 2D ANSYS calculations on the heat transport in the tungsten lamella: surface temperature reached after 10 sec heat flux exposure for different lamella wetted fractions.
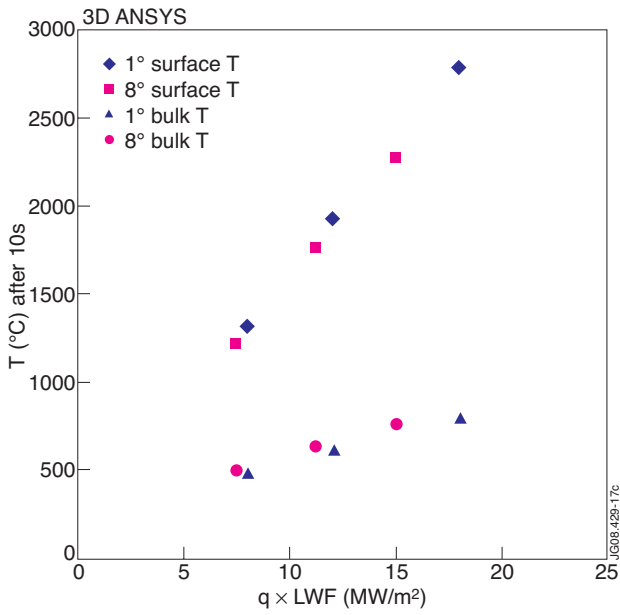
Figure 17: 3D ANSYS calculations on the heat transport in the tungsten lamella: surface and bulk temperature reached after 10s heat flux exposure for different lamella wetted fractions.
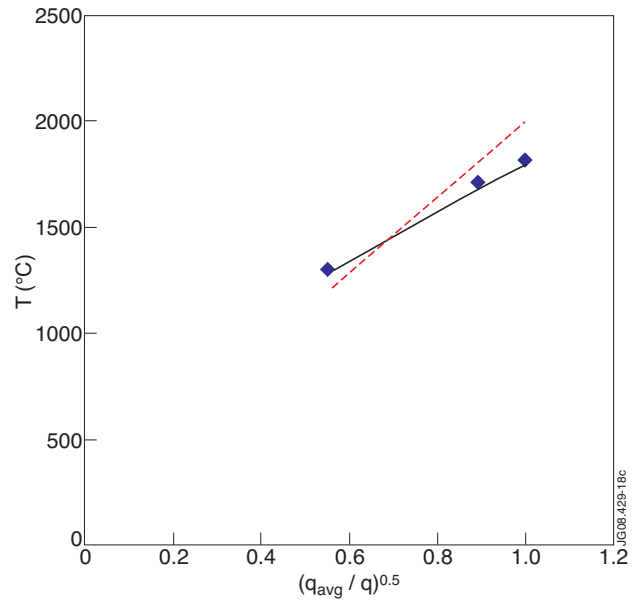

Figure 18: 3D ANSYS calculations on the heat transport in the tungsten lamella: surface temperature reached after 10s heat flux exposure for different ratios of average heat flux to peak heat flux density, meaning for different magnetic flux expansions or power flux decay length.
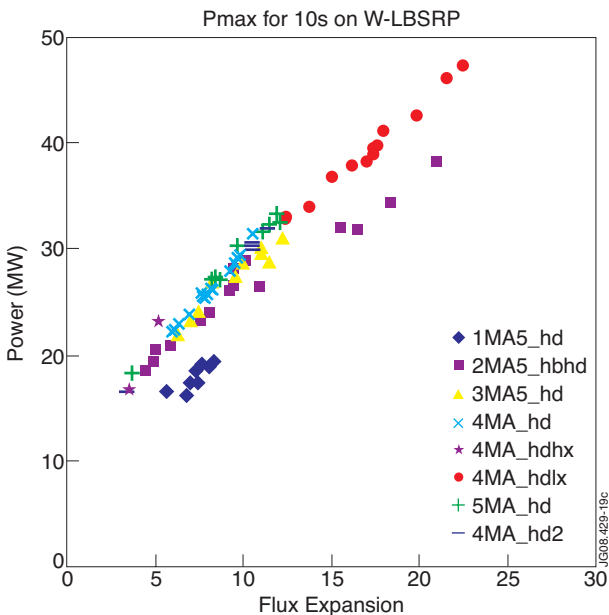

Figure 19: Maximum power for a 10 sec plasma pulse on the W-LBSRP before the maximum surface temperature is reached for static configurations versus the flux expansion of the individual magnetic plasma configuration.
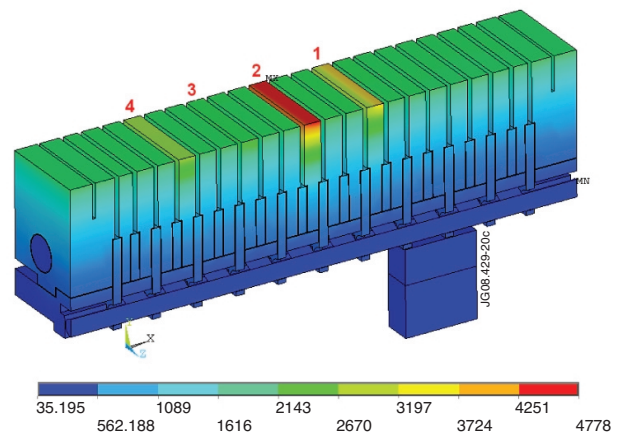

Figure 20: Temperature distribution in a complete stack of tungsten lamellae for different heat loads: (1) 20 MW/m2, (2) 30 MW/m2, (3) 12 MW/m2, (4) 16 MW/m2.
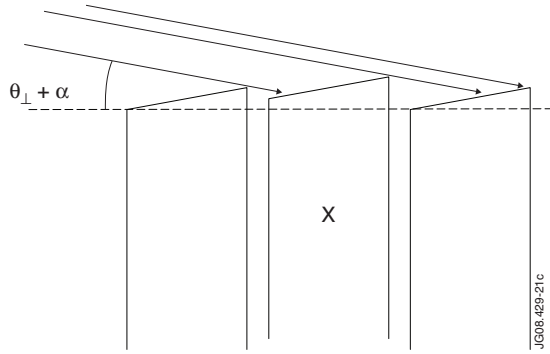
13

Figure 21: Schematic drawing of a misaligned lamella X and it's impact on the heat flux on the lamellae.
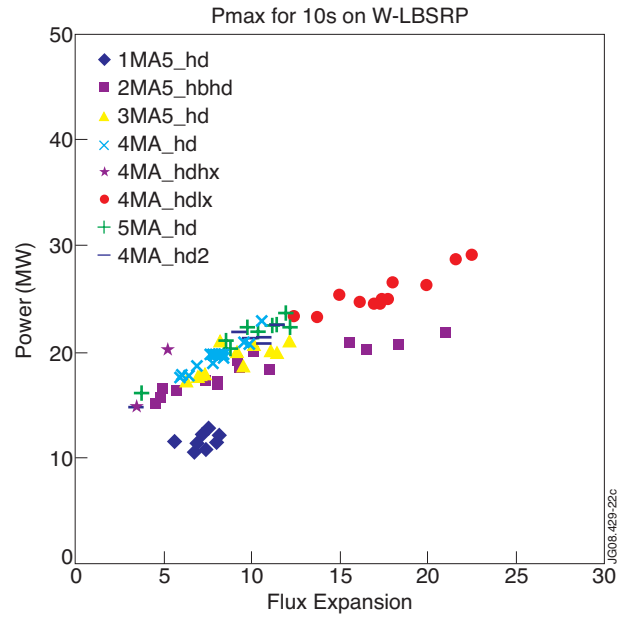

Figure 22: Maximum power for a 10s plasma pulse on the W-LBSRP before the maximum surface temperature is reached for static configurations versus the flux expansion of the individual magnetic plasma configuration taking into account a lamella manufacturing tolerance of $z=+-0.05mm$.